LAWRENCE
LIVERMORE
NATIONAL
LABORATORY

LLNL-JRNL-698176

Synergy between fast-ion transport by core MHD and test blanket module fields

W. W. Heidbrink, M. E. Austin, C. S. Collins, T. Gray, B. A. Grierson, G. J. Kramer, M. Lanctot, A. G. McLean, D. C. Pace, M. A. Van Zeeland

July 20, 2016

Nuclear Fusion

Disclaimer

This document was prepared as an account of work sponsored by an agency of the United States government. Neither the United States government nor Lawrence Livermore National Security, LLC, nor any of their employees makes any warranty, expressed or implied, or assumes any legal liability or responsibility for the accuracy, completeness, or usefulness of any information, apparatus, product, or process disclosed, or represents that its use would not infringe privately owned rights. Reference herein to any specific commercial product, process, or service by trade name, trademark, manufacturer, or otherwise does not necessarily constitute or imply its endorsement, recommendation, or favoring by the United States government or Lawrence Livermore National Security, LLC. The views and opinions of authors expressed herein do not necessarily state or reflect those of the United States government or Lawrence Livermore National Security, LLC, and shall not be used for advertising or product endorsement purposes.

Synergy between fast-ion transport by core MHD and test blanket module fields

W.W. Heidbrink,[1, a)] M.E. Austin,[2] C.S. Collins,[1] T. Gray,[3] B.A. Grierson,[4] G.J. Kramer,[4] M. Lanctot,[5] A.G. Mclean,[6] D.C. Pace,[5] and M.A. Van Zeeland[5]

[1)] *University of California Irvine, Irvine, California, USA*

[2)] *University of Texas at Austin, Austin, Texas, USA*

[3)] *Oak Ridge National Laboratory, Oak Ridge, Tennessee, USA*

[4)] *Princeton Plasma Physics Laboratory, Princeton, New Jersey, USA*

[5)] *General Atomics, San Diego, California, USA*

[6)] *Lawrence Livermore National Laboratory, Livermore, California, USA*

(Dated: 10 March 2015)

Fast-ion transport caused by the combination of MHD and a mock-up test-blanket module (TBM) coil is measured in the DIII-D tokamak. The primary diagnostic is an infrared camera that measures the heat flux on the tiles surrounding the coil. The combined effects of the TBM and four other potential sources of transport are studied: neoclassical tearing modes, Alfvén eigenmodes, sawteeth, and applied resonant magnetic perturbation fields for the control of edge localized modes. A definitive synergistic effect is observed at sawtooth crashes where, in the presence of the TBM, the localized heat flux at a burst increases from 0.36 ± 0.27 to 2.6 ± 0.5 MW/m^2.

PACS numbers: 52.55.Pi, 52.35.Bj

[a)] Electronic mail: Bill.Heidbrink@uci.edu

1. Introduction

The proposed ITER tritium-breeding test blanket modules (TBMs)[1] are expected to contain ferromagnetic materials that will perturb the nearby plasma with $\sim 1\%$ local magnetic field reductions. These field perturbations could cause concentrated losses of alpha particles that damage the wall near the TBMs. Calculations[2] indicate that, in the absence of additional fast-ion transport mechanisms, the alpha loss power fraction will be very low, $\sim 0.2\%$. The calculated losses are tiny because the perturbing fields are most effective at the plasma edge, where the production of alpha particles is small. However, the concern remains that instabilities may transport alpha particles from the populated core region to the plasma edge, where the TBM fields are effective[2] (Fig. 1). The combined effect of MHD modes and of TBM fields could be much more dangerous than either in isolation because the TBM fields may concentrate nearly axisymmetric losses from MHD into localized "hot spots." The present experiment investigates this possibility.

The experiment uses the mock-up TBM field coils that were previously installed on DIII-D[3]. Although three TBM modules are planned for ITER, the DIII-D mock-up coils are installed at a single toroidal location. To mimic the ITER fields, the DIII-D installation contains two racetrack coils and a vertical solenoid that are both energized in the present experiment. The amplitude of the perturbed field exceeds the amplitude of a single ITER TBM by a factor of ~ 3.

Previous experiments found that the mock-up TBM fields degrade both fusion product[3] and beam-ion[4] confinement. During beam injection, localized heating on the graphite tiles that surround the TBM port is observed[4]. Initially, it was unclear whether this additional heating is caused by beam-ion impact or by increased heat flux from the bulk plasma but, in a follow-up experiment[5], 2 MW of beam power was replaced by 3.3 MW of electron cyclotron heating power in plasmas with the same plasma shape. Localized heating was only observed during neutral beam injection, definitively establishing that beam-ion losses are responsible.

The strategy in the present experiment is straightforward: With the TBM either on or off, compare the localized heat flux in plasmas with identical MHD. In some cases, these comparisons are performed in sequential discharges while, in others, comparisons are possible at different times in the same discharge (Fig. 2). Ideally, to establish synergistic transport between the MHD and the TBM fields, MHD-quiescent discharges with the TBM either on or off would also be obtained but this was generally not possible without altering the plasma conditions.

This paper is organized as follows. After an overview of the DIII-D apparatus (Sec. 2), the synergy data between TBM fields and four different perturbing fields are presented. Section 3 is about

synergy with transport by neoclassical tearing modes (NTM), Section 4 is about Alfvén eigenmode (AE) induced transport, Section 5 is about transport by sawteeth, and Section 6 is about transport in the presence of combined TBM and resonant magnetic perturbation (RMP) fields. Since a major goal of the present study is to provide data for code benchmarking within the framework of the International Tokamak Physics Activity (ITPA) Topical Group on Energetic Particles, each section contains information on the MHD modes, core fast-ion transport, and localized heating. Section 6 summarizes the results.

2. Apparatus

All plasmas are deuterium discharges heated by deuterium neutral beams with injection energies of 74-81 keV. For these experiments, all of the beamlines are centered on the midplane. The near-perpendicular and near-tangential DIII-D sources have tangency radii of 0.76 m and 1.15 m, respectively. Carbon from the graphite walls is the dominant impurity.

The mock-up TBM coils are unchanged from the previous experiments[3,4,6], except that the apparatus was installed at a toroidal angle of 285° rather than at 270° (Fig. 3). Two sets of coils, the racetrack coil and the solenoid coil, mimic the toroidal and poloidal magnetization of a pair of ITER TBMs in one equatorial port. A current magnitude of 1 kA in both coils produces a spatially localized magnetic field perturbation that is largest on the low field side midplane. Near the plasma surface ($R = 2.29$ m), the peak radial, vertical, and toroidal magnetic field perturbations are 409, 340, and 129 G, respectively.

The primary diagnostic of fast-ion loss is an infrared (IR) camera that views the tiles surrounding the TBM coils (Fig. 3). The measured radiation is related to the tile temperature through calibration of the camera, lens and mirrors with a blackbody source. The heat flux is deduced from the surface temperature by a 1-D, semi-infinite model of heat conduction into the tile bulk[7]. When the TBM coils are energized, the temperature and inferred heat flux generally rise (Fig. 4). In this study, unless otherwise stated, the quoted heat flux is an average over the 2-3 pixels that are most sensitive to the TBM fields. The location of these pixels changes slightly with plasma conditions but, in all cases, corresponds to the upper right "hot spot" in Fig. 4.

DIII-D is also equipped with a pair of scintillator-based fast-ion loss detectors (FILD)[8] (Fig. 3). Light from the scintillator is split between a CCD camera that provides pitch and energy resolution and photomultipliers that provide excellent temporal resolution. The data in this paper are photomultiplier signals from a full-energy spot on the scintillator that observes prompt losses from the counter-injected beams.

Fast-ion D-alpha (FIDA) measurements are the primary diagnostic for the profile of confined fast ions. Most of the data presented here is from the system[9] with an oblique view (Fig. 3) that is primarily sensitive to co-passing ions. The spectra are integrated between 650.5-652.7 nm; this wavelength range corresponds to energies along the line-of-sight of 25-68 keV. The intensity calibration is obtained from an MHD-quiescent shot. The measurements are compared with the classical signals predicted by the synthetic diagnostic code FIDASIM[10] using the distribution function computed by NUBEAM[11]. The error bars are obtained by forming an ensemble of the ratio of measured brightness to predicted brightness at a series of time points, so both measurement errors and errors associated with plasma-profile uncertainties are included.

Typical plasma parameters for the four parts of the experiment appear in Fig. 5. The electron density (Fig. 5a) is measured by Thomson scattering[12] and CO_2 interferometers[13]. The electron temperature (Fig. 5b) is measured by Thomson scattering and an electron cyclotron emission (ECE) radiometer[14]. The ion temperature, rotation frequency, and Z_{eff} profiles (Figs. 5c-e) are inferred from charge exchange recombination spectroscopy measurements of carbon[15]. The safety factor profile (Fig. 5f) is from EFIT equilibrium reconstructions[16] that use magnetics and motional Stark effect[17] data.

The toroidal (n) and poloidal (m) mode numbers of the instabilities are measured by toroidal and poloidal arrays of magnetic probes[18], while radial profiles are from ECE electron temperature fluctuation measurements.

3. Synergy with Neoclassical Tearing Modes

The plasma shape for the NTM experiments is an elongated ($\kappa \simeq 1.8$), high triangularity ($\delta \simeq 0.6$), divertor configuration (Fig. 3b). The "outer gap" between the last-closed flux surface and the wall is a relatively large 9.6 cm in these plasmas. The plasma is an H-mode plasma with edge localized modes (ELM). As in previous experiments[19], a series of beam power steps is used to trigger an $m = 2$, $n = 1$ (2/1) tearing mode at ~ 1900 ms (Fig. 6). This creates a relatively stationary plasma with a large NTM that has a fairly steady frequency of ~ 10 kHz between ~ 2500-3800 ms. During this stationary phase, an average beam power of 5.2 MW is injected, with 9% in the counter-tangential direction, 32% in the co-perpendicular direction, and 59% in the co-tangential direction. The TBM coils are energized on some shots but not on others; the mode amplitude is unaffected by the TBM. On some shots, the power burst fails to trigger an NTM.

Figure 7 shows the radial profile of the NTM from ECE. The fluctuation amplitude of $\delta T_e \sim$

80 eV implies a radial displacement of $\xi_R \simeq \delta T_e/\nabla T_e \simeq 3$ cm. The phase jumps $180°$ across the $q = 2$ surface, as expected for a resistive 2/1 mode.

If the NTM causes enhanced fast-ion transport, the effect is modest. Figure 8 shows FIDA profiles for three discharges in this series. The discharge without an NTM has the largest signal on the innermost FIDA channel but the difference is within the uncertainty. Similarly, compared to the classical prediction, the neutron rate is 2 and 9% larger on the discharge without an NTM relative to a pair of discharges with NTMs.

Application of the TBM fields to these discharges causes an increase in heat flux to the tiles surrounding the coils (Fig. 9, Table I). As expected, the discharge with neither TBM fields nor an NTM has the smallest heat flux. Even without TBM fields, the heat flux is enhanced by an NTM. For the two discharges with NTMs but no TBM, the heat flux signals differ considerably despite the fact that plasma parameters and MHD activity (NTM characteristics, ELMs, Alfvén eigenmodes) are similar in the two shots. In the discharge with the TBM, the heat flux increases from ~ 2 MW/m^2 to ~ 8 MW/m^2 when the TBM is energized. This temporal correlation strongly suggests the increase is caused by the TBM fields; indeed, changes are modest at this time in the "no TBM" reference shots. Unfortunately, a similar discharge with TBM fields but without an NTM was not obtained, so one cannot independently ascertain the contribution of NTM-induced transport to the enhanced heat flux.

If the TBM fields concentrate losses near the coils, this is likely to reduce the fast-ion losses elsewhere. This effect is clearly observed by the FILD diagnostic (Fig. 10). A beam injected in the counter-current direction produces prompt losses that are detected by the FILD. When the TBM coils are energized, the prompt loss signals are 3-4 times smaller than when the TBM coils are off.

4. Synergy with Alfvén Eigenmodes

The Alfvén eigenmode (AE) portion of the study used plasma conditions that are similar to many previous DIII-D experiments. Early beam injection during the current ramp of an L-mode plasma (Fig. 11) drives many toroidal AEs and reversed-shear AEs unstable[20]. The plasma shape is a slightly-elongated ($\kappa \simeq 1.3$) oval with a relatively small outer gap of 4.5 cm (Fig. 3b). An average power of 3.8 MW is injected, with 85% in the co-tangential direction and 15% in the counter-tangential direction. The TBM is energized on some shots but not on others. Strong fast-ion losses are detected by the FILD detectors early in the current ramp[21] (Fig. 11d). On some discharges, electron cyclotron heating (ECH) is applied near q_{min} in an attempt to alter the

amplitude of the RSAEs[22].

As is typical for these conditions, many small-amplitude AEs are observed, both RSAEs that sweep upward in frequency and TAEs with relatively steady frequencies (Fig. 12). These modes cause strong transport that flattens the fast-ion profile[23]. Figure 13 compares the measured FIDA signal to the expected signal as a function of major radius. In the central quarter of the plasma, the signal is $\lesssim 60\%$ of the classical prediction. Simulations suggest that stochastic diffusive transport by the AEs is responsible for the flattening[24]. Thus, these plasmas are likely to produce synergistic transport between core MHD and edge TBM fields.

Figure 14 compares data from five discharges, two with TBM fields and three without. The amplitude of the AE activity is unaffected by application of the TBM (Fig. 14a). The central fast-ion transport, as inferred from the volume-averaged neutron rate, is also insensitive to application of the TBM (Fig. 14b). But the heat flux to the tiles surrounding the TBM coils reproducibly increases by an order of magnitude when the TBM fields are present (Fig. 14d).

Unfortunately, a similar discharge with TBM fields but without AEs was *not* obtained, so it is impossible to distinguish between transport induced by the TBM coils alone and synergistic transport for this condition. A limited attempt was made to use ECH to alter the virulence of the AE activity but the effect on fast-ion transport was slight (as inferred from the neutron rate) and the heat flux was unaffected.

5. Synergy with Sawteeth

The synergy between fast-ion transport by sawteeth and TBM fields was studied in the second half of the AE discharges, during the current flattop (Fig. 11). The plasma shape remains a slightly-elongated oval with an outer gap of ~ 4 cm. To maintain the plasma in L-mode, a relatively low average power of 4.5 MW is injected, with 10% in the counter-tangential direction, 52% in the co-perpendicular direction, and 38% in the co-tangential direction. With an edge safety factor of $q_{95} = 3.4$, the $q = 1$ surface is at a normalized minor radius of $\rho \simeq 0.39$. Very regular sawteeth are observed.

Figure 15 shows details of a representative sawtooth. Both $n = 1$ precursors and $n = 1$ postcursors are observed on the magnetics (Fig. 15a). The mode grows explosively in the crash phase. Ninety percent of the drop in central electron temperature occurs in 12 μs (Fig. 15b). ECE measurements show that both the precursor and the postcursor have $m = 1$ structure (Fig. 15d). Within the $q = 1$ surface, the measured ECE amplitude of the precursor has approximately a

triangle shape (Fig. 15c). Taking into account the temperature gradient ∇T_e, the eigenfunction is roughly a "top-hat" inside $\rho \lesssim 0.2$ but increases in amplitude closer to the $q = 1$ surface.

Information on the amplitude of the displacement is obtained from the ECE data (Fig. 16). The amplitude of the precursor oscillations is ~ 15 cm peak-to-peak and grows very slowly between 2466-2468 ms. The explosive phase occurs in ~ 2 cycles, with a final peak-to-peak excursion of ~ 30 cm.

As in a previous study of fast-ion transport by sawteeth in DIII-D[25], the sawtooth crash transports fast ions from inside the $q = 1$ surface to outside $q = 1$. Figure 17 shows FIDA profiles before and after the sawtooth crash. Near the magnetic axis, the signal drops 25-30% while, outside $q = 1$, the signal rises. Previous work on both DIII-D[25] and elsewhere[26,27] indicate that passing particles usually suffer more transport than trapped particles.

Sawteeth cause increased heat flux to the wall (Fig. 18). Without TBM fields, the flux jumps up at each sawtooth crash, then gradually relaxes. A possible explanation for the slow recovery is that the sawtooth populates the outer portion of the plasma with fast ions that subsequently collisionally scatter onto loss orbits. (The energy-loss and pitch-angle-scattering times at $\rho = 0.8$ are ~ 85 and 250 ms, respectively.) Application of TBM fields to these discharges causes a large increase in heat flux to the tiles surrounding the TBM. Increases in the magnitude of the burst at the crash, in the average heat flux, and in the relaxation time following a crash are all observed.

For the four discharges in the experiment, the time-averaged heat flux is 3.5 ± 0.5 times larger with the TBM. In contrast, signals at other toroidal locations, such as FILD detectors or D-alpha light monitors, are unaffected by the TBM.

Figure 19 shows analysis of the bursts in heat flux at each sawtooth crash for the data in Fig. 18. For these data with drops in central temperature of 33-42%, the burst in heat flux is uncorrelated with the magnitude of the temperature drop (correlation coefficient $r = -0.02$) but is strongly correlated with the TBM current ($r = 0.91$). The jump in heat flux at a sawtooth is 2.6 ± 0.5 MW/m^2 when the TBM current exceeds 0.5 kA, compared to 0.36 ± 0.27 with the TBM off.

5. Synergy with Resonant Magnetic Perturbation (RMP) Fields

The DIII-D tokamak is equipped with a set of six internal coils (I-coils) above and below the midplane that are spaced uniformly in the toroidal direction and designed to make a radial field perturbation of up to 120 G at the coil location immediately behind the first wall. Application of

3D fields with the DIII-D internal coils ("I-coils") can suppress ELMs[28]. In the present experiment, ELMs are suppressed by $n = 3$ odd-parity RMP fields, then TBM fields are added to assess the effect on the concentrated heat flux.

Figure 20 shows a typical discharge. The plasma shape is a high-triangularity divertor, as in the NTM experiment (Fig. 3b). The outer gap is 7 cm. Large ELMs occur prior to application of the $n = 3$ field but these are suppressed approximately 300 ms after the field is applied (Fig. 20c). Normally, the $n = 3$ field is continuously applied but, in order to distinguish between TBM and $n = 3$ induced losses, 50-ms "notches" are applied to the I-coil waveforms (Fig. 20b). ELM suppression is sustained during these brief intervals. The density drops when the I-coil current is applied and begins to recover during the notches (Fig. 20a). Apart from a $\sim 35\%$ in toroidal rotation, application of the TBM fields has little effect on plasma parameters such as the stored energy or neutron rate. During the TBM pulse, an average power of 6.3 MW is injected, with 38% from co-perpendicular sources and 62% from co-tangential sources.

The effect of the $n = 3$ fields on fast-ion confinement (in the absence of TBM fields) is documented in a recent paper[29]. The $n = 3$ fields cause a $\sim 50\%$ reduction in FIDA channels outside $\rho \gtrsim 0.95$. Full-orbit modeling indicates that passing ions are most affected. Figure 21 shows similar FIDA data when the TBM is energized. With both I-coil and TBM fields, the FIDA signals are lower than without TBM fields but the effect is comparable to the uncertainty in the measurement.

Application of TBM fields causes a modest ~ 0.2 MW/m^2 increase in heat flux to the tiles (Fig. 22). Although the magnitude of the increase is modest, the fractional increase in the time-average heat flux is appreciable (a factor of 3.3 times larger with TBM). Both with and without the TBM, the flux decreases when the I-coil turns off for 50 ms, demonstrating that the $n = 3$ fields contribute to the localized heating. For the three "notches" in the I-coil field, the reduction in heat flux is $15 \pm 3\%$ without the TBM and $12 \pm 2\%$ with the TBM.

6. Summary and Discussion

Results of the four experiments are summarized in Table II. In all cases, TBM fields increase the time-averaged localized heat flux.

Increased heat flux does not by itself indicate a synergistic effect between MHD-induced transport and TBM-induced transport, as enhancements were previously observed that are not attributed to MHD[4,5]. Ideally, data would exist in these four quadrants:

1. no MHD, no TBM,

2. w/ MHD, no TBM,

3. no MHD, w/ TBM,

4. w/ MHD, w/ TBM.

Complete coverage of this sort was obtained for the sawtooth bursts and for the RMP experiment. Consequently, it can be definitely stated that the combination of fast-ion transport at the sawtooth crash with TBM fields resulted in an increase in concentrated losses (Fig. 19). In the RMP study, the peak heat flux with both $n = 3$ and TBM fields is $14 \pm 2\%$ larger with combined fields than with TBM fields alone.

The absence of quadrant #3 for the NTM and AE cases prevents a definitive demonstration of synergistic transport for these cases. In light of the large AE-induced transport measured in the core (Fig.13), it seems very likely that the TBM heat flux was enhanced by the Alfvén eigenmodes but there is no proof that this is the case. For the NTM condition, the concentrated heat flux is relatively large even prior to application of the TBM, suggesting that the NTM plays a role in fast-ion transport. When the TBM is applied, the heat flux rapidly increases (Fig. 9) and the FILD signal decreases (Fig. 10), further suggesting synergistic transport. On the other hand, the modest changes in core fast-ion confinement (Fig. 8) suggest that other factors besides synergistic transport could be operative.

The implications of these data for ITER are beyond the scope of this paper. The purpose of this paper is to provide well-documented cases for benchmarking of computer codes. The data for all four cases are posted at the ITPA Energetic Particle website[30]. Successful benchmarking against DIII-D experimental data will improve the reliability of ITER predictions. Concentrated losses of alphas at sawteeth in the ITER baseline scenario is a particularly important issue for future research.

ACKNOWLEDGMENTS

This work was supported by the U.S. Department of Energy under SC-G903402, ??? DE-FG03-97ER54415, DE-AC05-0000R22725, DE-AC02-09CH11466, and DE-FC02-04ER54698,. We thank R. Nazikian and C. Petty for helpful suggestions and the entire DIII-D team for their support.

Prepared by LLNL under Contract DE-AC52-07NA27344.

REFERENCES

[1]GINACARLI, L. et al., Fusion Eng. Des. **85** (2010) 1829.

[2]SHINOHARA, K., KURKI-SUONIO, T., SPONG, D., et al., Nucl. Fusion **51** (2011) 063028.

[3]SCHAFFER, M. J., SNIPES, J. A., GOHIL, P., et al., Nucl. Fusion **51** (2011) 103028.

[4]KRAMER, G. J., BUDNY, B. V., ELLIS, R., et al., Nucl. Fusion **51** (2011) 103028.

[5]KRAMER, G. J., MCLEAN, A., BROOKS, N., et al., Nucl. Fusion **53** (2013) 123018.

[6]KRAMER, G. J., BUDNY, R. V., BORTOLON, A., et al., Plasma Phys. Controlled Fusion **55** (2013) 025013.

[7]CARSLAW, H. S. and JAEGER, J. C., *Conduction of Heat in Solids*, Oxford University Press, New York, 1959.

[8]FISHER, R. K., PACE, D. C., GARCÍA-MUNOZ, et al., Rev. Sci. Instrum. **81** (2010) 10D307.

[9]MUSCATELLO, C. M., HEIDBRINK, W. W., TAUSSIG, D., and BURRELL, K. H., Rev. Sci. Instrum. **81** (2010) 10D316.

[10]HEIDBRINK, W. W., LIU, D., LUO, Y., RUSKOV, E., and GEIGER, B., Comm. Comp. Physics **10** (2011) 716.

[11]PANKIN, A., MCCUNE, D., ANDRE, R., BATEMAN, G., and KRITZ, A., Comp. Phys. Comm. **159** (2004) 157.

[12]CARLSTROM, T. N., CAMPBELL, G. L., DEBOO, J. C., et al., Rev. Sci. Instrum. **63** (1992) 4901.

[13]CARLSTROM, T. N., AHLGREN, D. R., and CROSBIE, J., Rev. Sci. Instrum. **59** (1988) 1063.

[14]AUSTIN, M. E. and LOHR, J., Rev. Sci. Instrum. **74** (2003) 1457.

[15]GOHIL, P., BURRELL, K. H., GROEBNER, R. J., and SERAYDARIAN, R. P., Rev. Sci. Instrum. **61** (1990) 2949.

[16]LAO, L. L., ST. JOHN, H., STAMBAUGH, R. D., KELLMAN, A. G., and PFEIFFER, W., Nucl. Fusion **25** (1985) 1611.

[17]RICE, B. W., NILSON, D. G., and WROBLEWSKI, D., Rev. Sci. Instrum. **66** (1995) 373.

[18]STRAIT, E. J., Rev. Sci. Instrum. **77** (2006) 023502.

[19]PETTY, C. C., LA HAYE, R. J., LUCE, T. C., et al., Nucl. Fusion **44** (2004) 243.

[20]VAN ZEELAND, M. A., KRAMER, G. J., AUSTIN, M. E., et al., Phys. Rev. Lett. **97** (2006) 135001.

[21]PACE, D. C., FISHER, R. K., GARCÍA-MUÑOZ, M., HEIDBRINK, W. W., and VAN ZEELAND, M. A., Plasma Phys. Controlled Fusion **53** (2011) 062001.

[22]VAN ZEELAND, M. A., HEIDBRINK, W. W., NAZIKIAN, R., et al., Plasma Phys. Controlled Fusion **50** (2008) 035009.

[23]HEIDBRINK, W. W., GORELENKOV, N. N., LUO, Y., et al., Phys. Rev. Lett. **99** (2007) 245002.

[24]WHITE, R. B., GORELENKOV, N., HEIDBRINK, W. W., and VANZEELAND, M. A., Plasma Phys. Controlled Fusion **52** (2010) 045012.

[25]MUSCATELLO, C. M., HEIDBRINK, W. W., KOLESNICHENKO, Y. I., et al., Plasma Phys. Controlled Fusion **54** (2012) 025006.

[26]NIELSEN, S. K., SALEWSKI, M., BINDSLEV, H., et al., Nucl. Fusion **51** (2011) 063014.

[27]GEIGER, B., GARCIA-MUNOZ, M., DUX, R., et al., Nucl. Fusion **54** (2014) 022005.

[28]EVANS, T. E., MOYER, R. A., THOMAS, P. R., et al., Phys. Rev. Lett. **92** (2004) 235003.

[29]VAN ZEELAND, M. et al., IAEA NF paper.

[30]ITPA website.

[31]HEIDBRINK, W. W., FERRON, J. R., HOLCOMB, C. T., et al., Plasma Phys. Controlled Fusion **56** (2014) 095030.

Tables

Shot	2200-2400 ms	2500-2650 ms
157401	0.42 (no NTM)	0.60 (no NTM)
157399	1.98	2.66
157400	4.48	6.93
157402	1.56	7.74 (TBM)

TABLE I. Time-averaged heat flux (in MW/m^2) for the four discharges shown in Fig. 9. Discharge #157401 (first row) did not have an NTM. The only entry with TBM fields is in the lower right corner.

Field	w/o TBM (MW/m^2)	w/ TBM (MW/m^2)	w/o Time (s)	w/ Time (s)
NTM	1.6-6.9	7.7	2.2-2.4	2.5-2.65
AE	0.2-0.4	2.8-2.9	0.9-1.0	0.9-1.0
Sawtooth	0.8-2.0	2.7-5.8	2.2-2.4	2.5-2.7
RMP	0.04	0.13	3.3-4.5	3.3-4.5

TABLE II. IR camera measurements of the time-averaged heat flux for the four experiments. The range in observed values for different discharges of the same type is given. The last two columns list the selected averaging intervals.

Figure Captions

Figure 1. Concept of the experiment. Transport of fast ions by core MHD to the edge region can populate the edge region, where TBM fields cause concentrated losses.

Figure 2. Overview of the experimental strategy. In each portion of the experiment, a different type of MHD (a-c) or applied field (d) causes transport. Either successive discharges with or without TBM fields are compared (a,b,d) or, in the case of sawteeth (c), the time period before and after the TBM pulse is compared with the period with TBM fields.

Figure 3. (a) Plan view and (b) elevation of the DIII-D tokamak, showing the locations of the TBM coils, the IR camera, one of the FILD detectors, the 40-channel ECE array, and the sightlines of the oblique FIDA diagnostic. The plasma shapes for the four experiments are also shown.

Figure 4. IR camera data for (a,b) temperature and (c,d) inferred heat flux without (a,c) and with (b,d) TBM fields in the NTM experiment at times 2260 and 3020 ms.

Figure 5. Time-averaged profiles of (a) n_e, (b) T_e, (c) T_i, (d) toroidal rotation frequency, (e) Z_{eff}, and q vs. ρ for the NTM (dashed line), AE (thick line), sawtooth (thin line) and RMP (dash-dot line) experiments.

Figure 6. (a) Line-averaged density, (b) central electron temperature, (c) $n = 1$ magnetics signal, (d) FILD photomultiplier signal, (e) neutron rate, and (f) injected beam power for a discharge in the NTM experiment. The period when the TBM field is applied on some of the discharges is indicated. TBM solenoid current $I_{TBM} = 0.91$ kA.

Figure 7. ECE measurements of the radial mode structure of the NTM. The position of the $q = 2$ surface inferred from the equilibrium reconstruction is indicated by the solid vertical lines; the dotted line represents the magnetic axis.

Figure 8. Ratio of FIDA signals to classical FIDASIM predictions vs. major radius between 2500-3000 ms for three discharges in the NTM experiment. The inset shows the classical beam density profiles predicted by NUBEAM.

Figure 9. (a) NTM mode amplitude, (b) TBM current, and (c) heat flux vs. time for four discharges in the NTM experiment.

Figure 10. FILD photomultiplier signal during NTM shots with and without TBM fields. The timing of the counter-injected beam is also shown.

Figure 11. (a) Line-averaged density, (b) central electron temperature, (c) plasma current, (d) FILD photomultiplier signal, (e) neutron rate, and (f) injected beam power for a discharge in the AE and sawtooth experiments. The periods when the TBM field and ECH power are applied on some of the discharges are indicated. TBM solenoid current during AE phase: $I_{TBM} = 0.86$ kA. TBM solenoid current during sawtooth phase: $I_{TBM} = 1.04$ kA.

Figure 12. Alfvén eigenmode activity measured by the cross-power of two interferometer signals in one of the AE discharges.

Figure 13. Ratio of FIDA signals to classical FIDASIM predictions between 350-750 ms vs. major radius. The inset shows the classical beam density profiles predicted by NUBEAM.

Figure 14. (a) AE mode amplitude[31], (b) ratio of measured neutron rate to NUBEAM prediction, (c) TBM current, and (d) heat flux vs. time for five discharges in the AE experiment.

Figure 15. Time evolution of (a) a magnetics signal and (b) $T_e(0)$ at a sawtooth crash. (c) Amplitude and (d) phase of the precursor prior to the explosive growth and the postcursor after the crash as measured by ECE. The dashed line shows the average value of $|\nabla T_e|$ (a.u.). The frequency of the precursor (postcursor) is 8.8 (8.3) kHz.

Figure 16. Contours of electron temperature vs. time and major radius for the same sawtooth as in Fig. 15. The dashed line represents the position of the magnetic axis.

Figure 17. FIDA signal before and after the sawtooth crash shown in Figs. 15 and 16. The temperature inflection point measured by ECE is indicated by the vertical line.

Figure 18. (a) Central electron temperature, TBM current, ECCD power, and (b) heat flux vs. time for four discharges in the sawtooth experiment. The dashed lines show time-averaged values that appear in Table II. The vertical line with arrows shows a heat-flux burst that is plotted in Fig. 19.

Figure 19. Jump in heat flux at sawtooth crashes vs. TBM current.

Figure 20. (a) Line-averaged density, (b) I-coil and TBM currents, (c) divertor D-alpha signal, (d) neutron rate, and (e) injected beam power for a discharge in the RMP experiment. TBM solenoid current $I_{TBM} = 1.06$ kA.

Figure 21. FIDA signal divided by injected neutral density vs. time for four tangentially viewing channels near the plasma edge. (The normalized minor radius is indicated.) The FIDA spectra are integrated from 659.5-661.5 nm. The I-coil waveform is also indicated. The dashed line represents the FIDA signals at $\rho \simeq 1.0$ in the corresponding "no-TBM" discharge, #157545.

Figure 22. (a) I-coil and TBM coil currents and (b) heat flux vs. time in a pair of discharges with and without TBM fields.

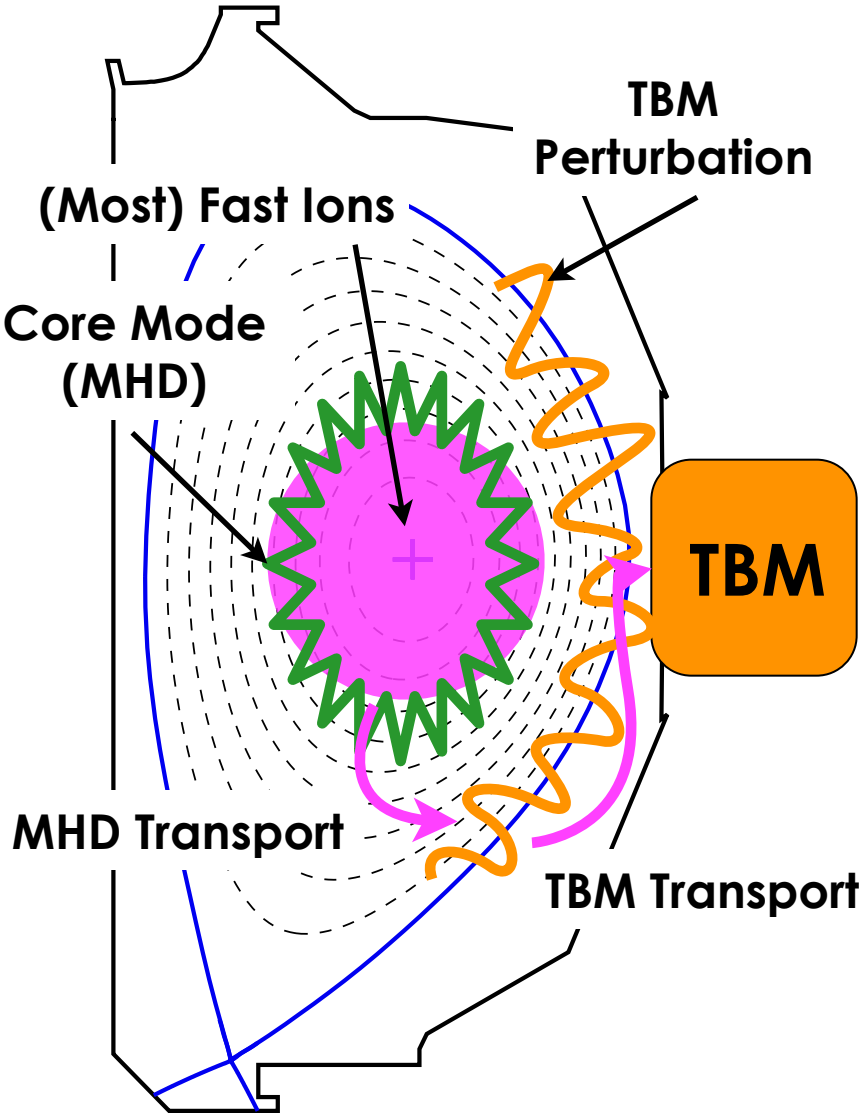
TBM
Perturbation
(Most) Fast Ions
Core Mode
(MHD)
TBM
MHD Transport
TBM Transport

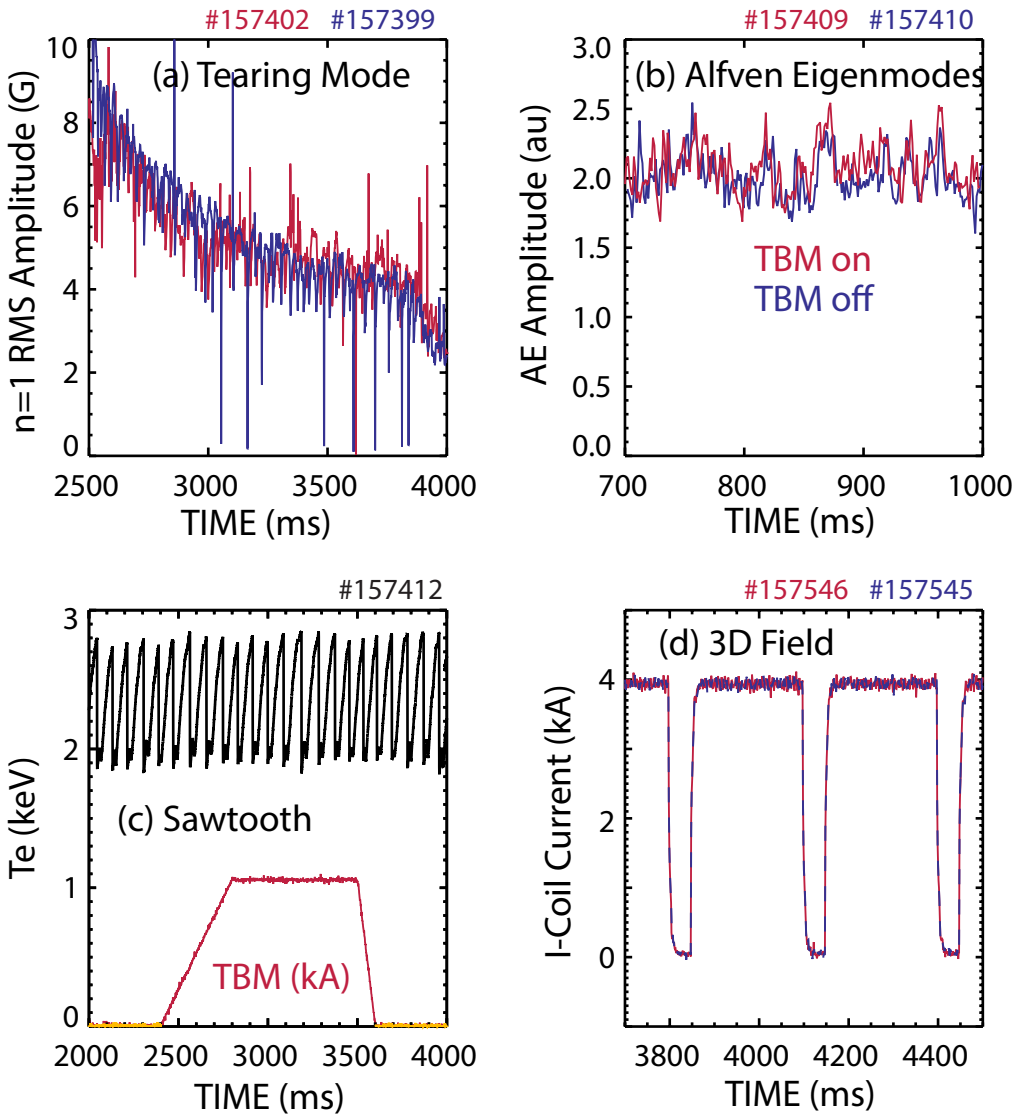
#157402 #157399
(a) Tearing Mode
n=1 RMS Amplitude (G)
TIME (ms)
#157409 #157410
(b) Alfven Eigenmodes
AE Amplitude (au)
TBM on
TBM off
TIME (ms)
#157412
(c) Sawtooth
Te (keV)
TBM (kA)
TIME (ms)
#157546 #157545
(d) 3D Field
I-Coil Current (kA)
TIME (ms)

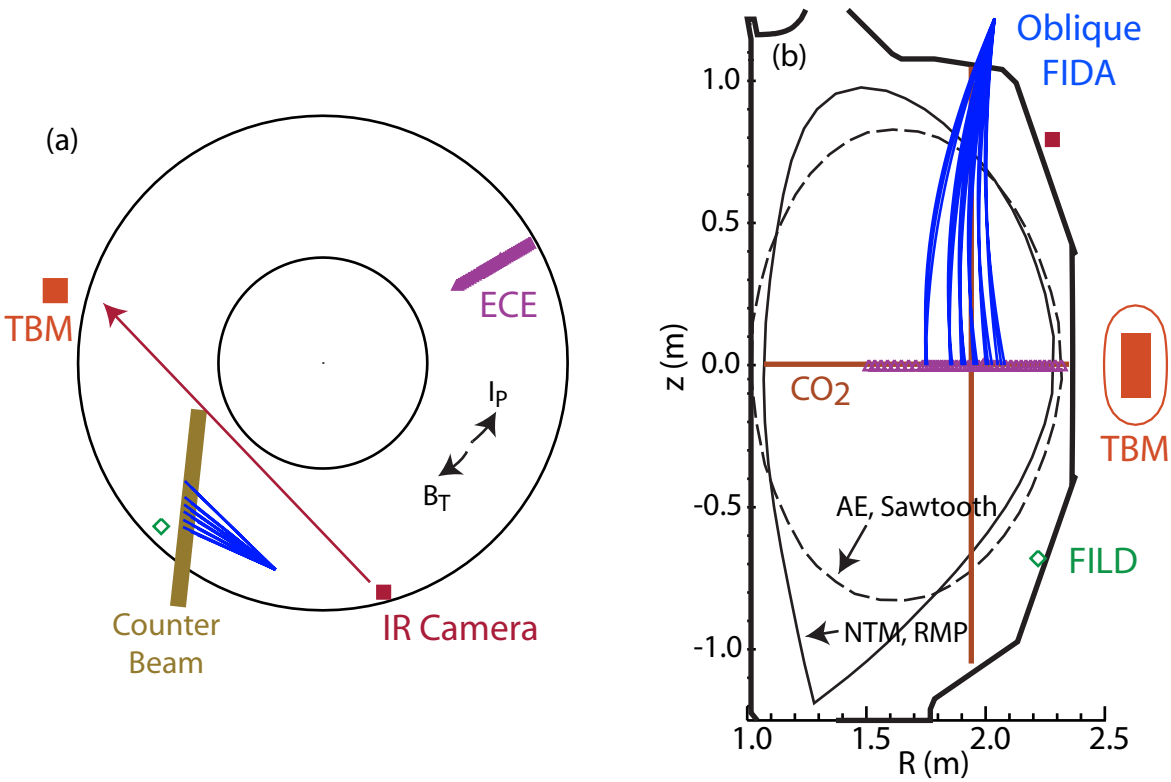
(a)
TBM
ECE
I_P
B_T
Counter
Beam
IR Camera
(b)
Oblique
FIDA
1.0
0.5
0.0
-0.5
-1.0
z (m)
CO_2
TBM
AE, Sawtooth
FILD
NTM, RMP
1.0
1.5
2.0
2.5
R (m)

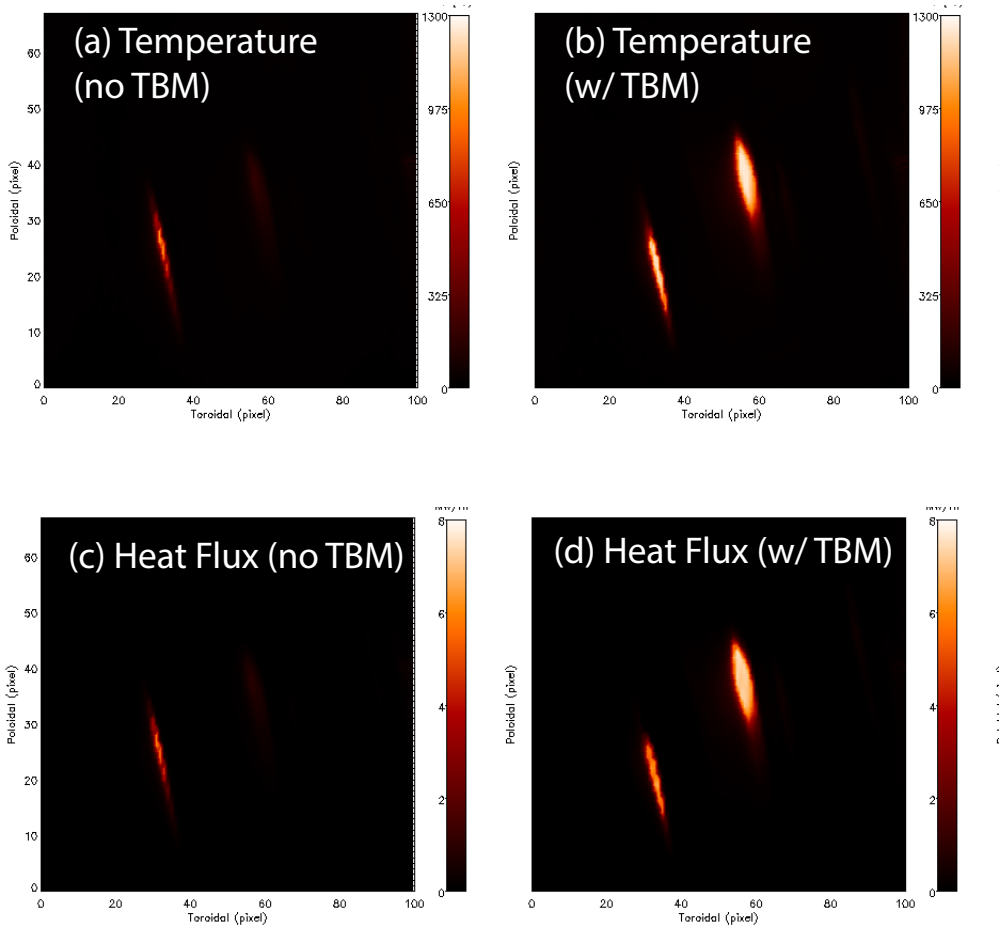
(a) Temperature
(no TBM)
(b) Temperature
(w/ TBM)
(c) Heat Flux (no TBM)
(d) Heat Flux (w/ TBM)
Poloidal (pixel)
Toroidal (pixel)
0
10
20
30
40
50
60
0
20
40
60
80
100
1300
975
650
325
0
8
6
4
2
0

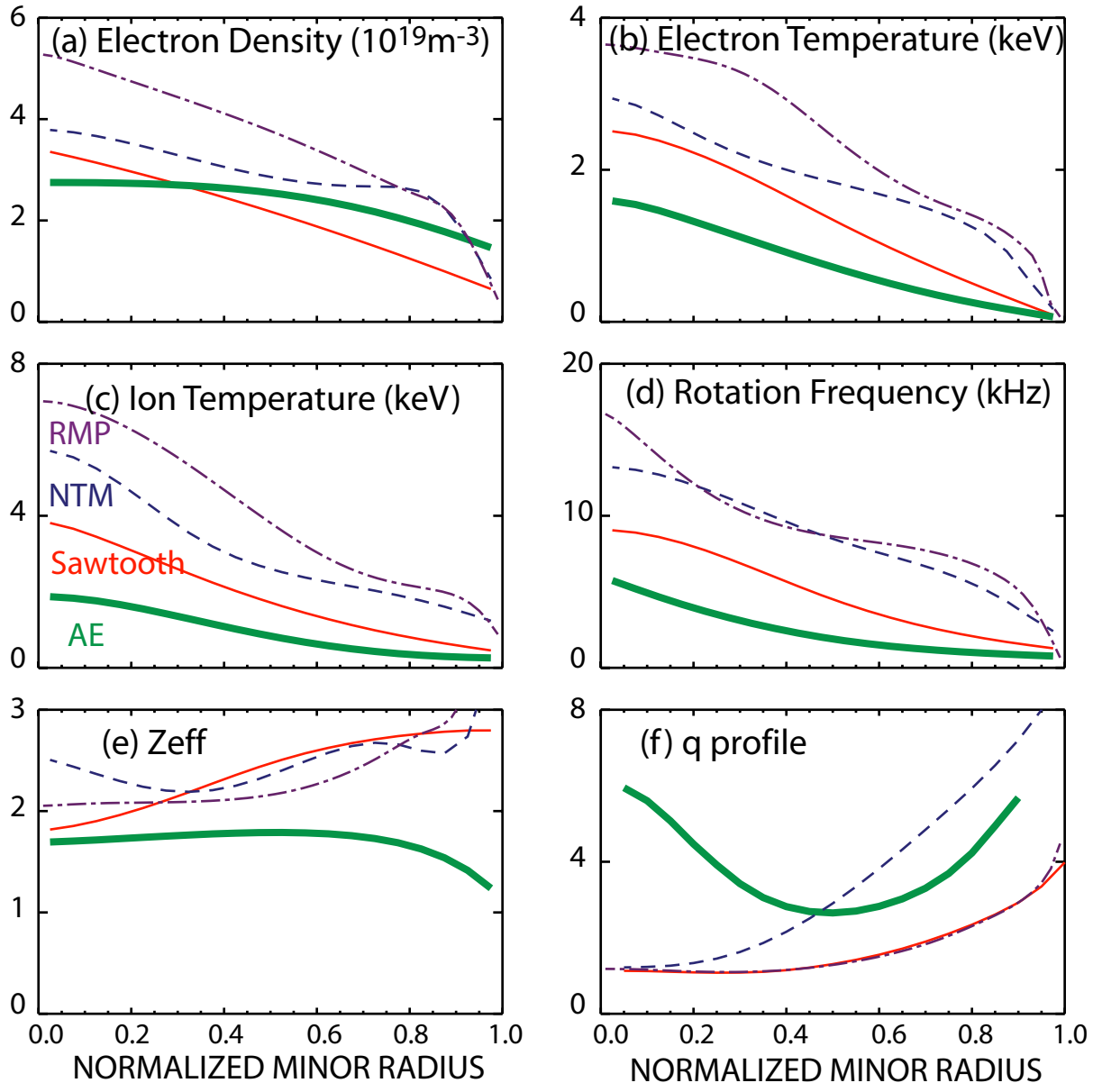
(a) Electron Density ($10^{19}m^{-3}$)
(b) Electron Temperature (keV)
(c) Ion Temperature (keV)
(d) Rotation Frequency (kHz)
(e) Zeff
(f) q profile
RMP
NTM
Sawtooth
AE
NORMALIZED MINOR RADIUS
NORMALIZED MINOR RADIUS

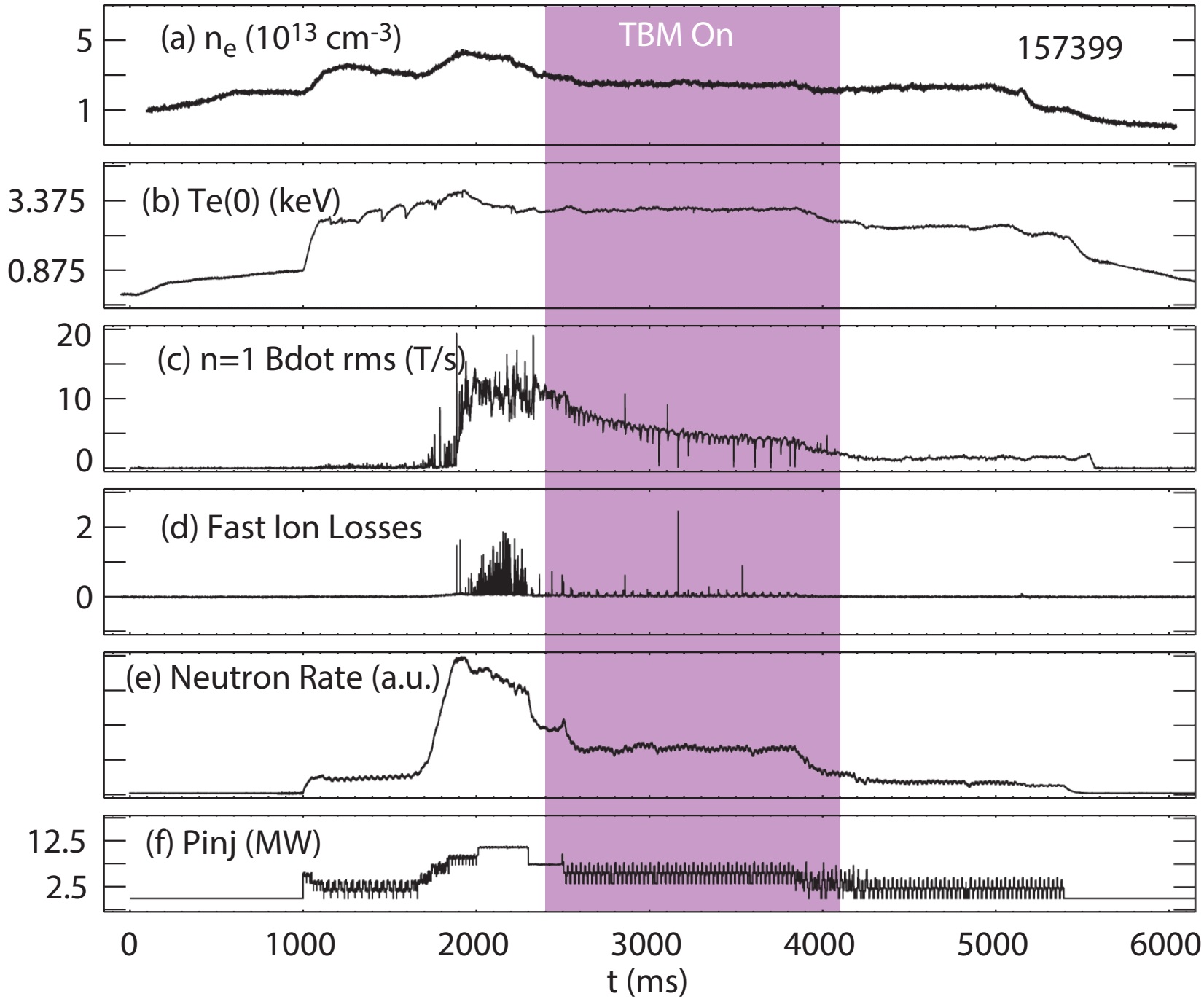
(a) n_e (10^{13} cm^{-3})
TBM On
157399
5
1
(b) Te(0) (keV)
3.375
0.875
(c) n=1 Bdot rms (T/s)
20
10
0
(d) Fast Ion Losses
2
0
(e) Neutron Rate (a.u.)
(f) Pinj (MW)
12.5
2.5
0
1000
2000
3000
4000
5000
6000
t (ms)

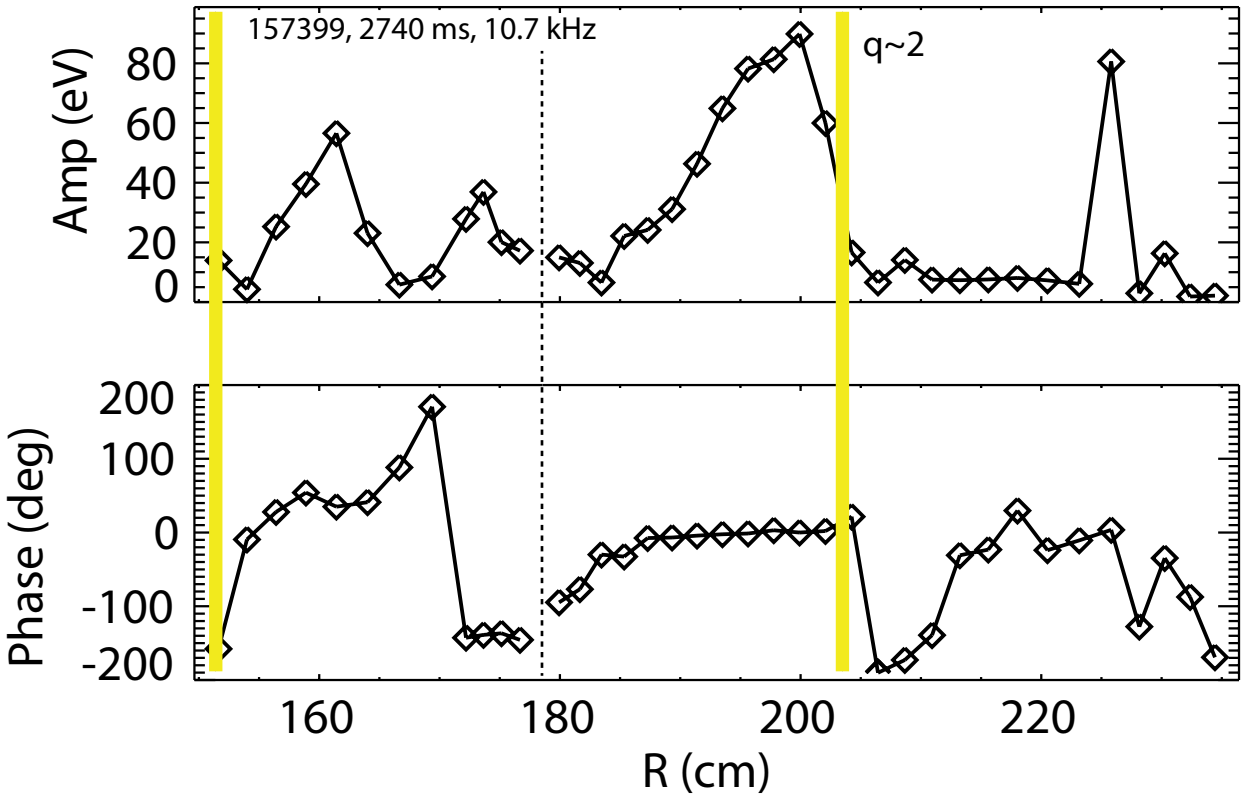
157399, 2740 ms, 10.7 kHz
q~2
Amp (eV)
80
60
40
20
0
Phase (deg)
200
100
0
-100
-200
160
180
200
220
R (cm)

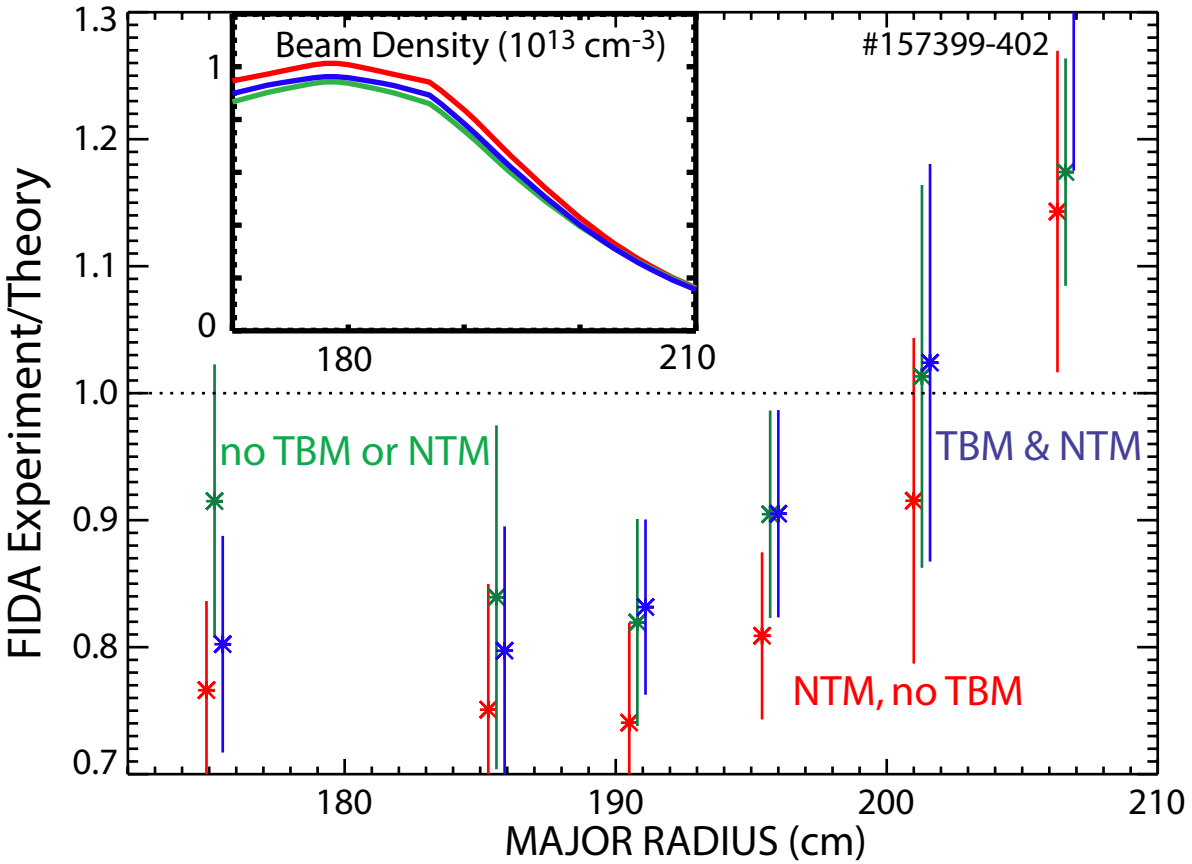
Beam Density (10^{13} cm^{-3})
1
0
180
210
#157399-402
FIDA Experiment/Theory
1.3
1.2
1.1
1.0
0.9
0.8
0.7
no TBM or NTM
TBM & NTM
NTM, no TBM
180
190
200
210
MAJOR RADIUS (cm)

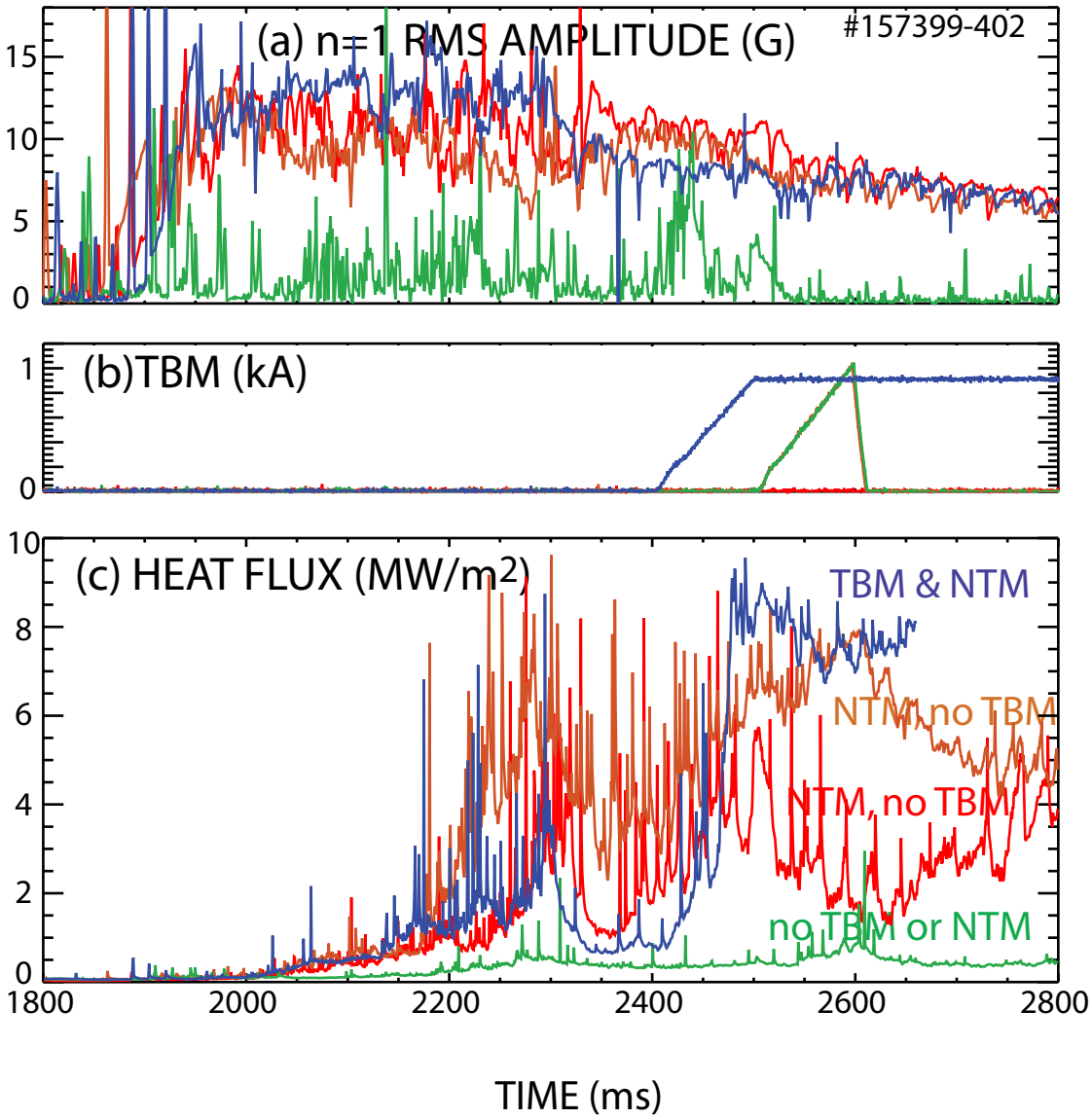
(a) n=1 RMS AMPLITUDE (G)
#157399-402
15
10
5
0
(b)TBM (kA)
1
0
(c) HEAT FLUX (MW/m2)
TBM & NTM
NTM, no TBM
NTM, no TBM
no TBM or NTM
10
8
6
4
2
0
1800
2000
2200
2400
2600
2800
TIME (ms)

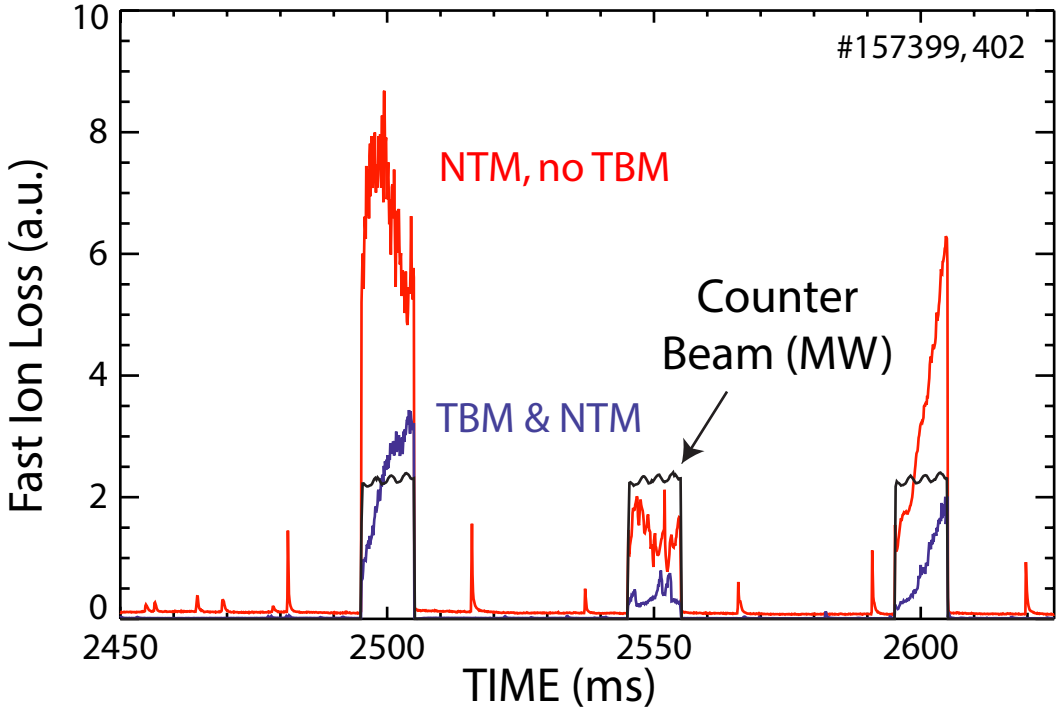
#157399, 402
NTM, no TBM
TBM & NTM
Counter
Beam (MW)
Fast Ion Loss (a.u.)
TIME (ms)
0
2
4
6
8
10
2450
2500
2550
2600

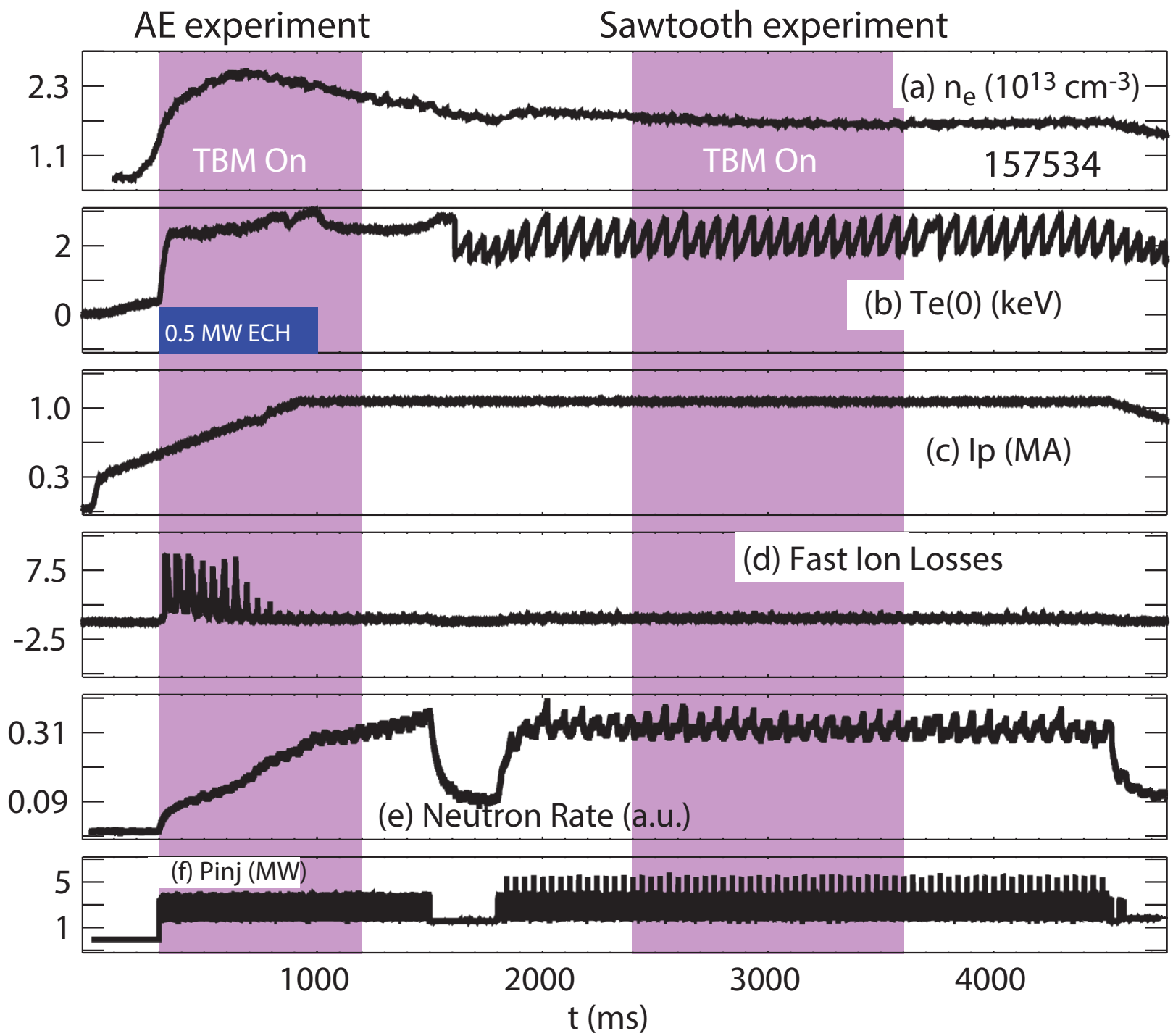
AE experiment
Sawtooth experiment
2.3
1.1
TBM On
TBM On
(a) n_e (10^{13} cm^{-3})
157534
2
0
0.5 MW ECH
(b) Te(0) (keV)
1.0
0.3
(c) Ip (MA)
7.5
-2.5
(d) Fast Ion Losses
0.31
0.09
(e) Neutron Rate (a.u.)
5
1
(f) Pinj (MW)
1000
2000
3000
4000
t (ms)

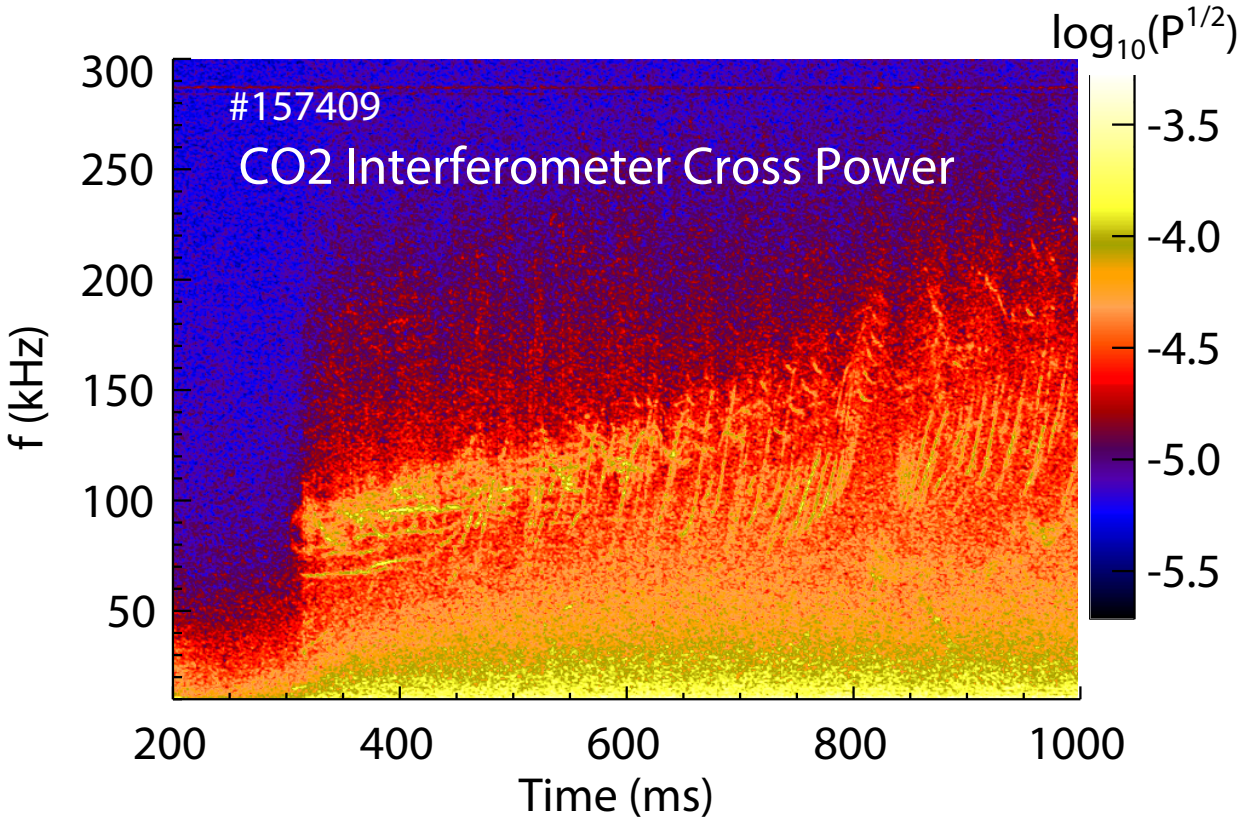
#157409
CO2 Interferometer Cross Power
f (kHz)
300
250
200
150
100
50
200
400
600
800
1000
Time (ms)
log10(P1/2)
-3.5
-4.0
-4.5
-5.0
-5.5

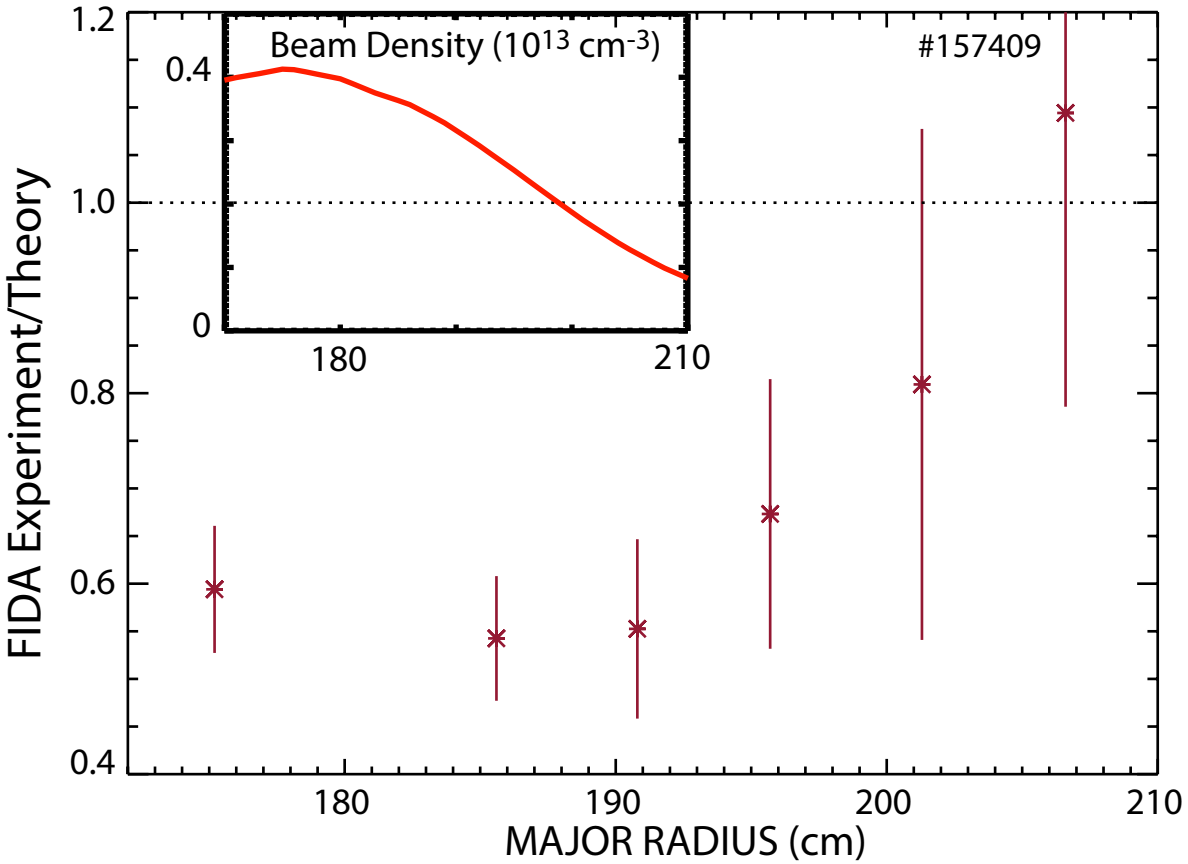
Beam Density (10^{13} cm^{-3})
0.4
0
180
210
#157409
1.2
1.0
0.8
0.6
0.4
FIDA Experiment/Theory
180
190
200
210
MAJOR RADIUS (cm)

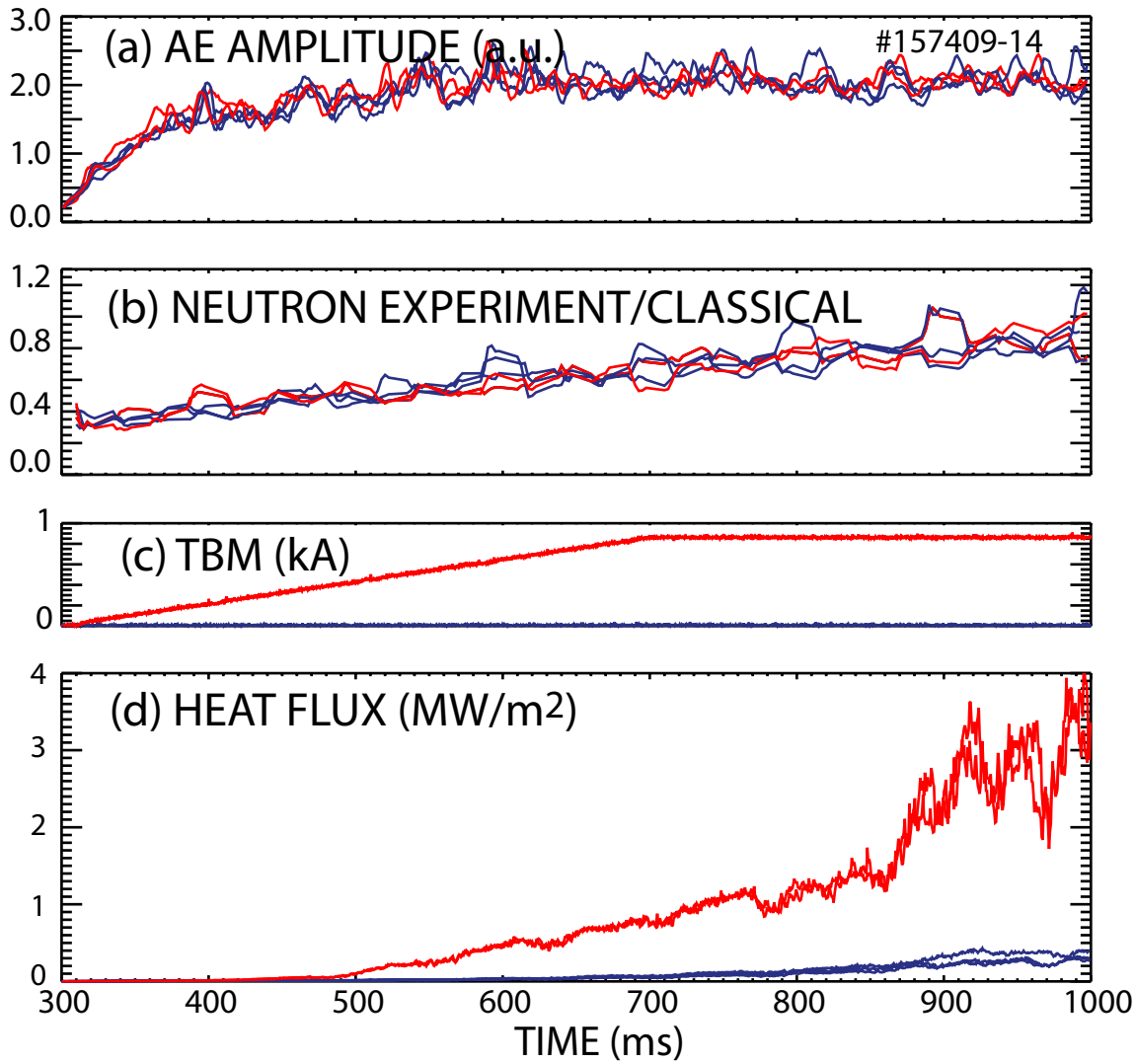
(a) AE AMPLITUDE (a.u.)
#157409-14
3.0
2.0
1.0
0.0
(b) NEUTRON EXPERIMENT/CLASSICAL
1.2
0.8
0.4
0.0
(c) TBM (kA)
1
0
(d) HEAT FLUX (MW/m2)
4
3
2
1
0
300
400
500
600
700
800
900
1000
TIME (ms)

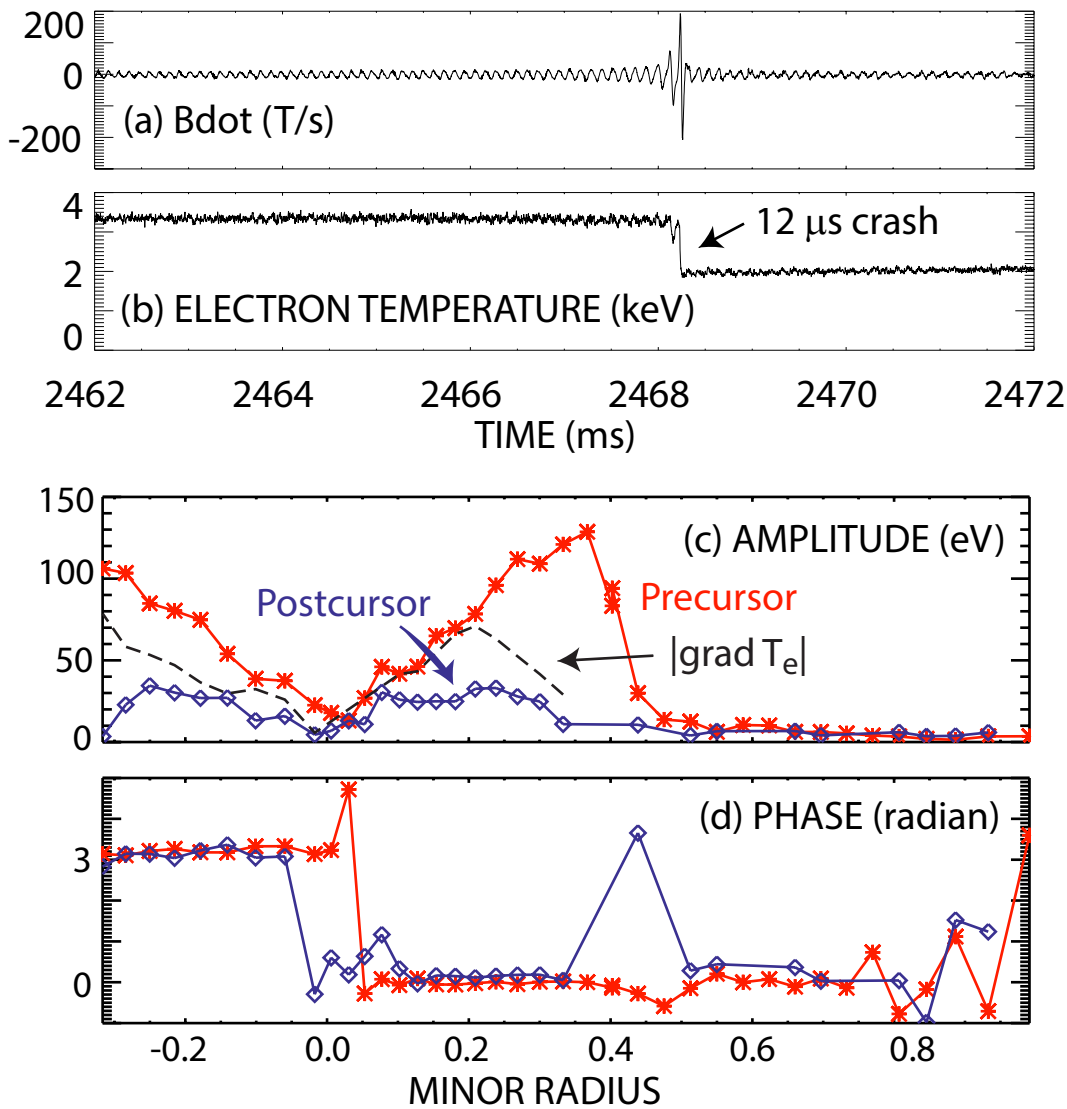
200
0
-200
(a) Bdot (T/s)
4
2
0
12 μs crash
(b) ELECTRON TEMPERATURE (keV)
2462
2464
2466
2468
2470
2472
TIME (ms)
150
100
50
0
(c) AMPLITUDE (eV)
Postcursor
Precursor
|grad Te|
3
0
(d) PHASE (radian)
-0.2
0.0
0.2
0.4
0.6
0.8
MINOR RADIUS

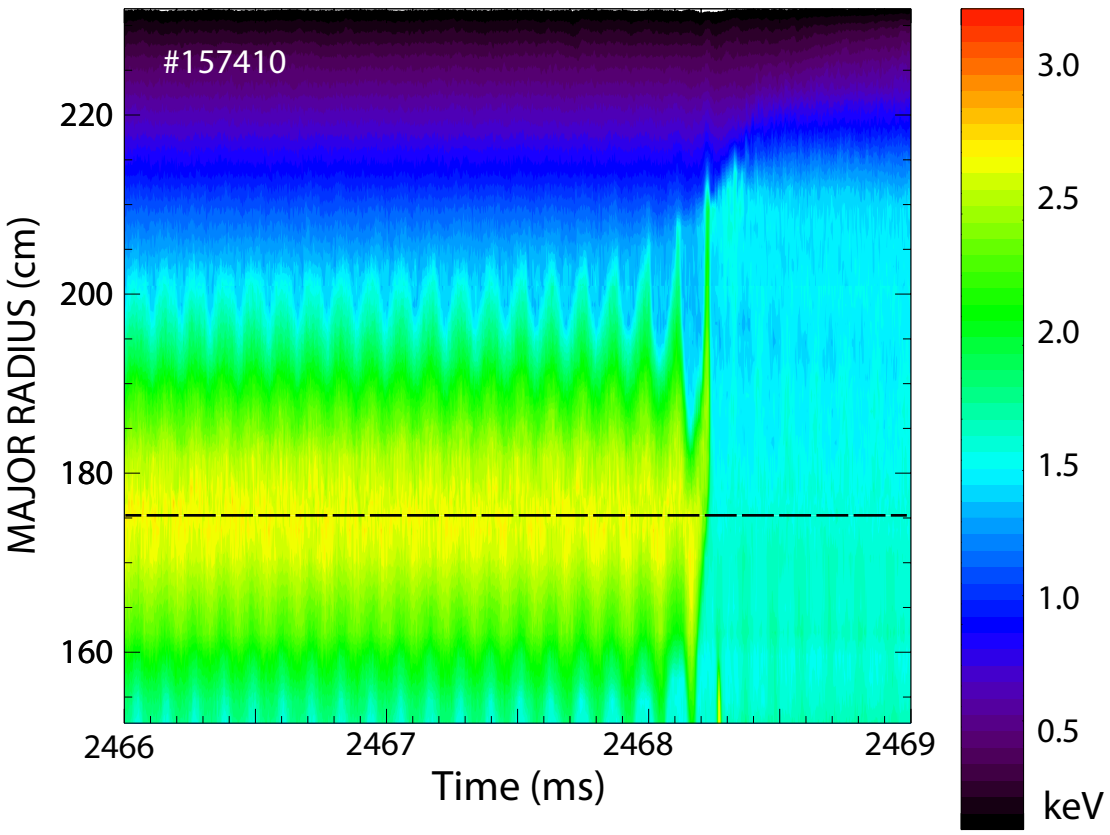
#157410
MAJOR RADIUS (cm)
220
200
180
160
2466
2467
2468
2469
Time (ms)
3.0
2.5
2.0
1.5
1.0
0.5
keV

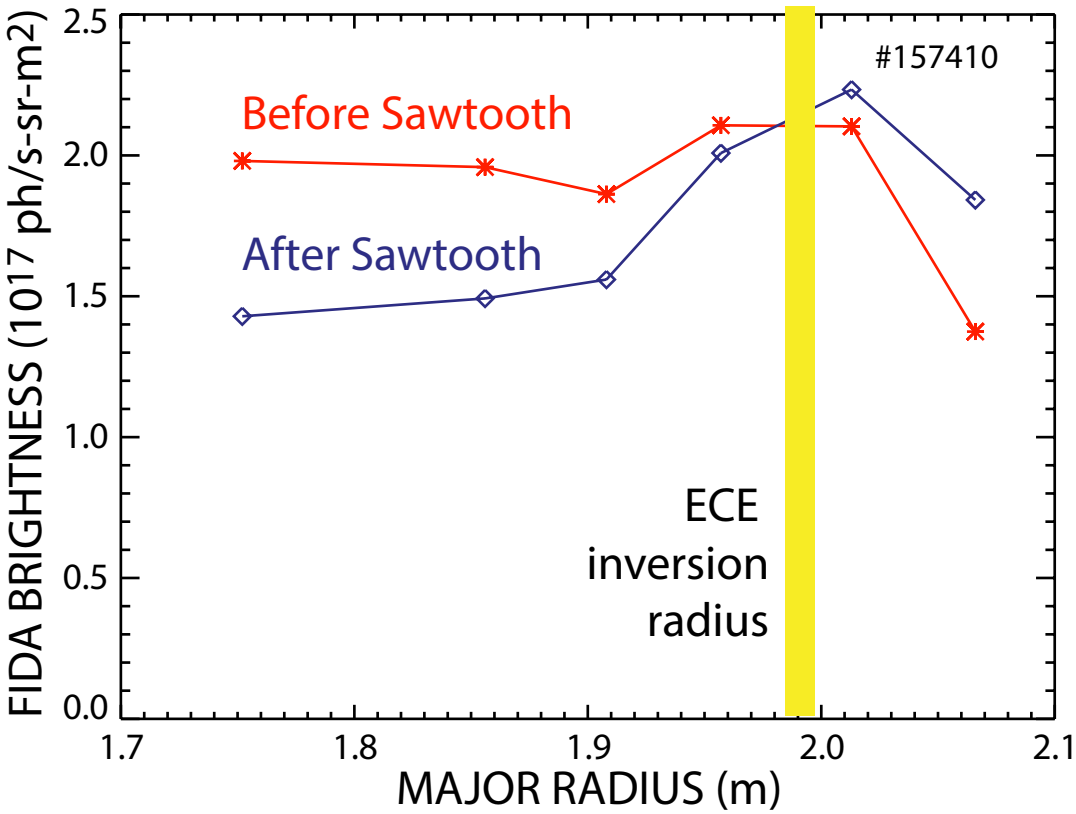
#157410
Before Sawtooth
After Sawtooth
ECE
inversion
radius
FIDA BRIGHTNESS (10^17 ph/s-sr-m^2)
MAJOR RADIUS (m)
2.5
2.0
1.5
1.0
0.5
0.0
1.7
1.8
1.9
2.0
2.1

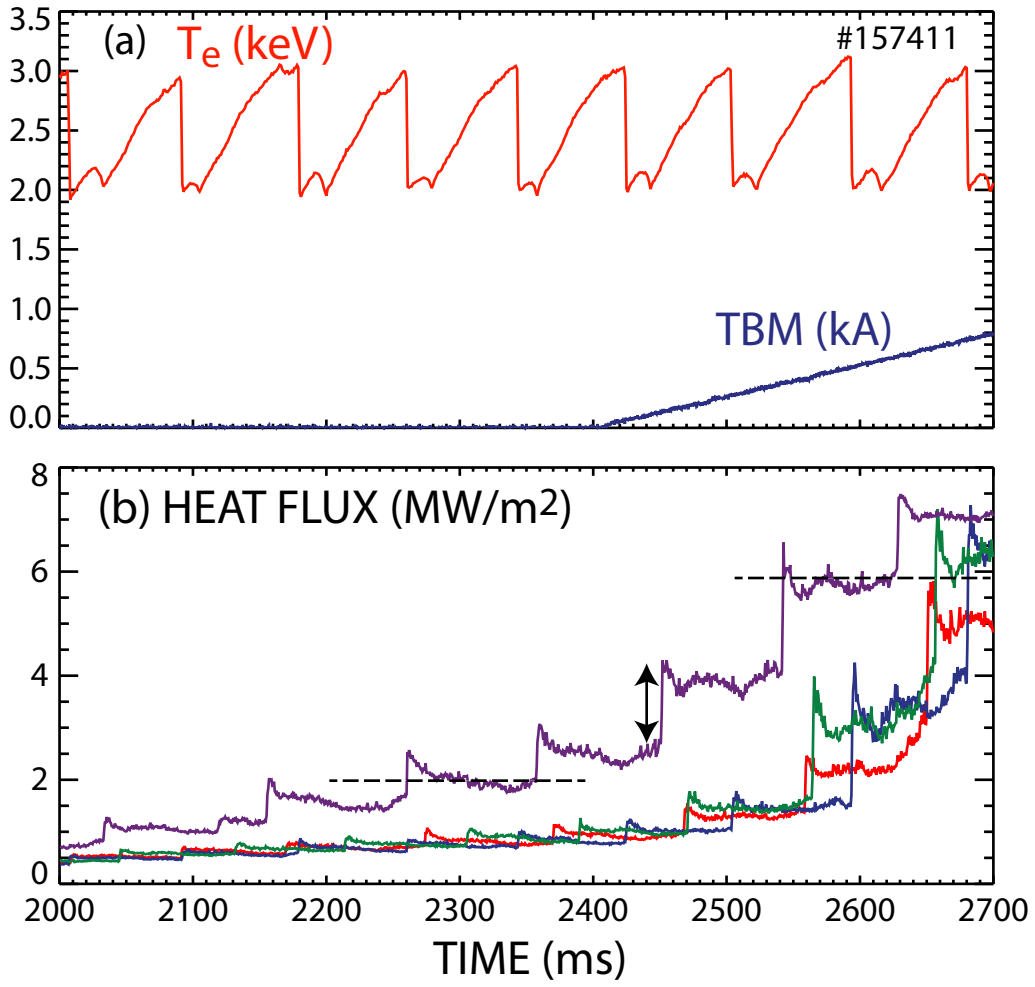
(a)
T_e (keV)
#157411
TBM (kA)
3.5
3.0
2.5
2.0
1.5
1.0
0.5
0.0
(b) HEAT FLUX (MW/m2)
8
6
4
2
0
2000
2100
2200
2300
2400
2500
2600
2700
TIME (ms)

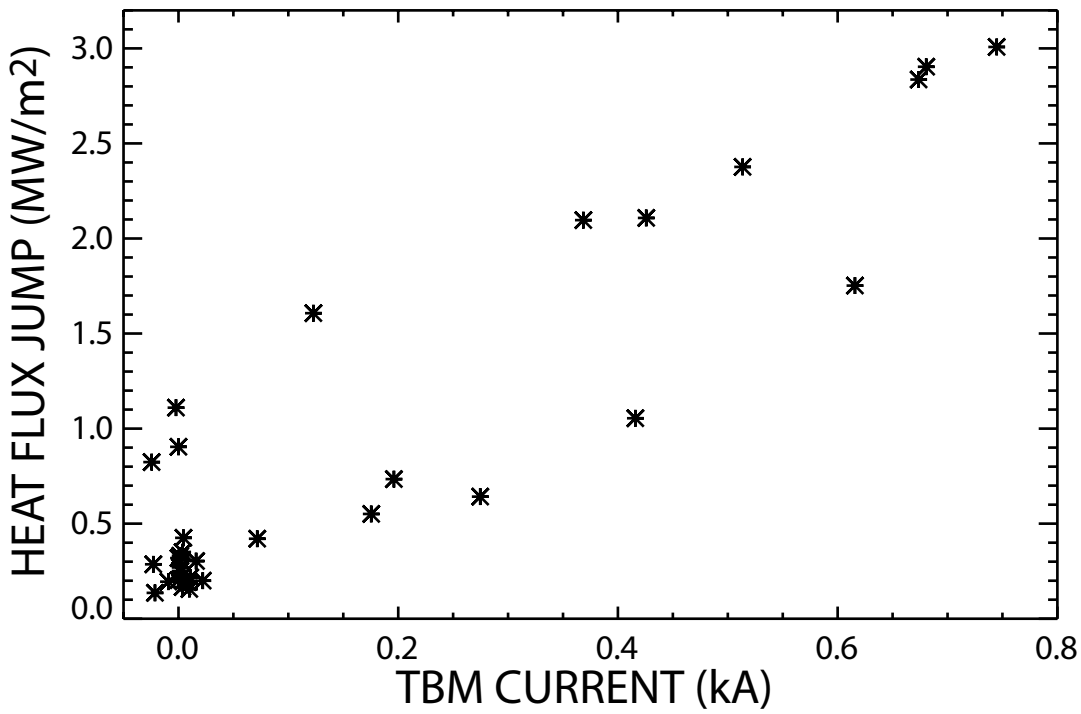
HEAT FLUX JUMP (MW/m2)
3.0
2.5
2.0
1.5
1.0
0.5
0.0
0.0
0.2
0.4
0.6
0.8
TBM CURRENT (kA)

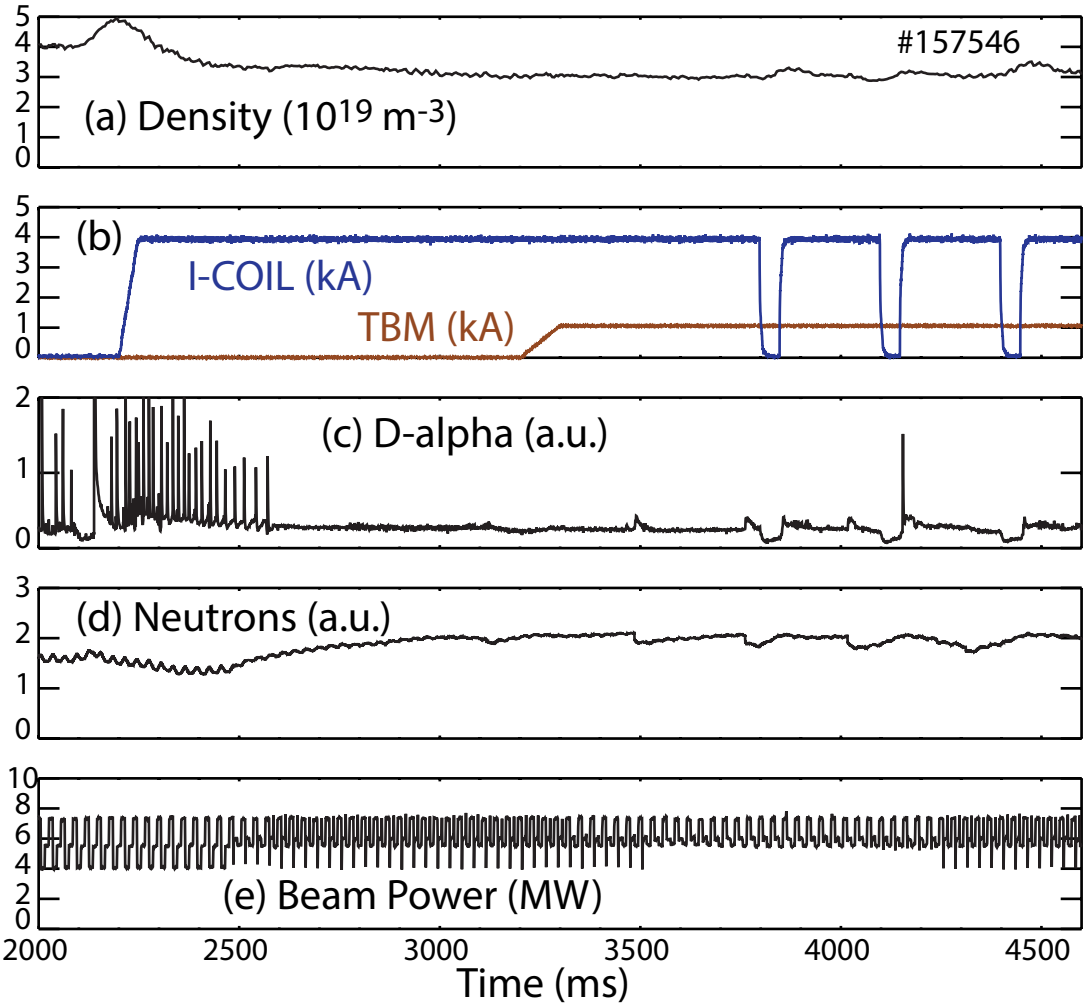
#157546
(a) Density (10^{19} m^{-3})
(b)
I-COIL (kA)
TBM (kA)
(c) D-alpha (a.u.)
(d) Neutrons (a.u.)
(e) Beam Power (MW)
2000
2500
3000
3500
4000
4500
Time (ms)

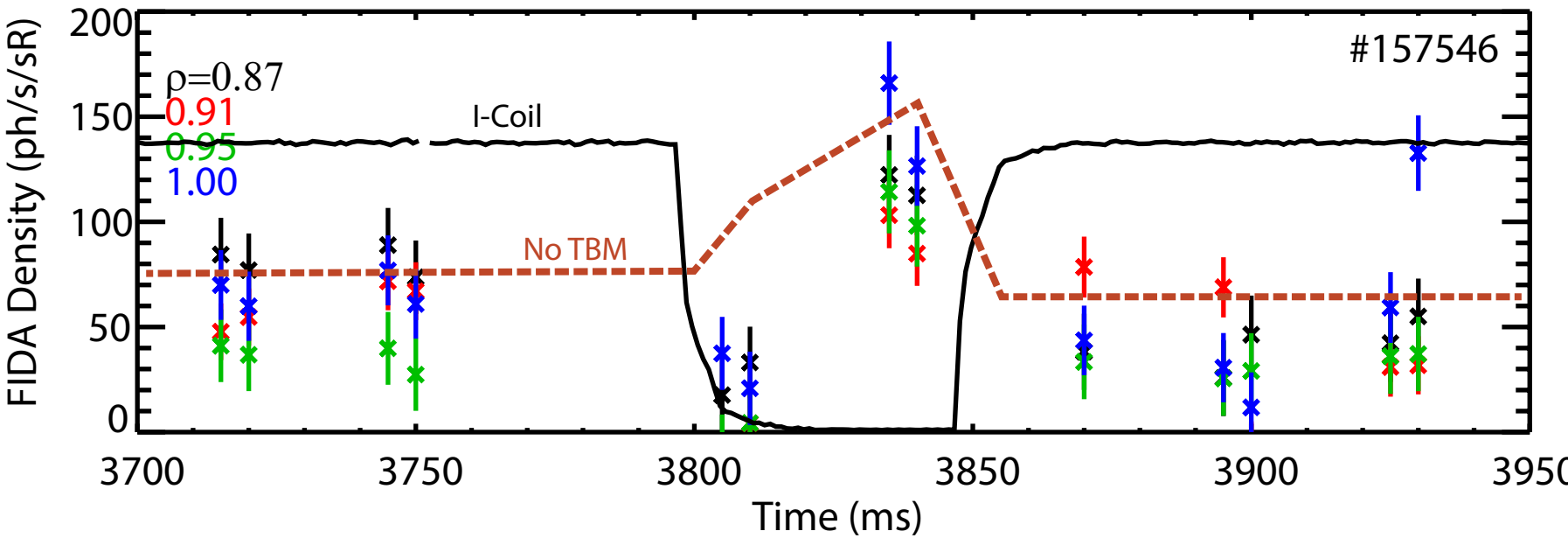
#157546
ρ=0.87
0.91
0.95
1.00
I-Coil
No TBM
FIDA Density (ph/s/sR)
Time (ms)
200
150
100
50
0
3700
3750
3800
3850
3900
3950

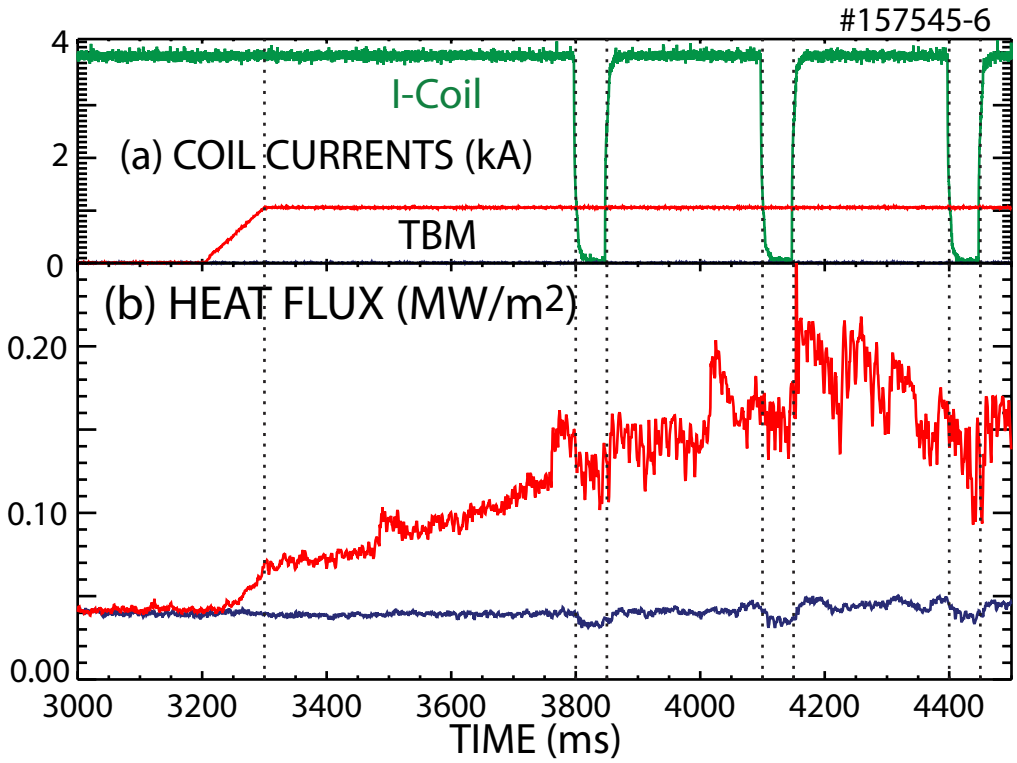
#157545-6
I-Coil
(a) COIL CURRENTS (kA)
TBM
(b) HEAT FLUX (MW/m2)
4
2
0
0.20
0.10
0.00
3000
3200
3400
3600
3800
4000
4200
4400
TIME (ms)